First observations of triple-frequency radar Doppler spectra in snowfall: Interpretation and applications

AGU PUBLICATIONS

Geophysical Research Letters

RESEARCH LETTER
10.1002/2015GL067618

Key Points:
- First analysis of triple-frequency Doppler radar spectra of rimed and unrimed snowfall
- Unique signature can be derived which characterized snowfall scattering properties
- Signature of riming can be well reproduced by recent calculations with discrete dipole approximation

Supporting Information:
- Table S1

Correspondence to:
S. Kneifel,
skneifel@meteo.uni-koeln.de

Citation:
Kneifel, S., P. Kollias, A. Battaglia, J. Leinonen, M. Maahn, H. Kalesse, and F. Tridon (2016), First observations of triple-frequency radar Doppler spectra in snowfall: Interpretation and applications, *Geophys. Res. Lett.*, *43*, 2225–2233, doi:10.1002/2015GL067618.

Received 8 JAN 2016
Accepted 12 FEB 2016
Accepted article online 14 FEB 2016
Published online 2 MAR 2016

First observations of triple-frequency radar Doppler spectra in snowfall: Interpretation and applications

S. Kneifel[1], P. Kollias[2], A. Battaglia[3], J. Leinonen[4], M. Maahn[1], H. Kalesse[5], and F. Tridon[3]

[1]Institute for Geophysics and Meteorology, University of Cologne, Cologne, Germany, [2]Department of Atmospheric and Oceanic Sciences, McGill University, Montreal, Quebec, Canada, [3]Department of Physics and Astronomy, University of Leicester, Leicester, UK, [4]Jet Propulsion Laboratory, California Institute of Technology, Pasadena, California, USA, [5]Leibniz Institute for Tropospheric Research, Leipzig, Germany

Abstract The potential of multifrequency Doppler spectra to constrain precipitation microphysics has so far only been exploited for dual-frequency spectra in rain. In this study, we extend the dual-frequency concept to triple-frequency Doppler radar spectra obtained during a snowfall event which included rimed and unrimed snow aggregates. A large selection of spectra obtained from low-turbulence regions within the cloud reveals distinctly different signatures of the derived dual spectral ratios. Due to the third frequency, a characteristic curve can be derived which is almost independent of the underlying particle size distribution and velocity-size relation. This approach provides new opportunities for validating existing and future snow scattering models and reveals how the information content of triple-frequency radar data sets can be further exploited for snowfall studies.

1. Introduction

The interpretation of radar-based snowfall measurements and their inversion to microphysical parameters is challenging due to the large natural variability in snowfall properties (e.g., particle size distribution (PSD), density, and shape) and uncertainty in the backscatter cross section of large, irregular snow particles [e.g., *Kulie and Bennartz*, 2009; *Szyrmer et al.*, 2012]. Multifrequency radar methods for snowfall utilize frequencies where snowflakes transition from the Rayleigh to the Mie scattering regime (e.g., X, Ku, Ka, or W band); this transition is dependent mainly on the relation of radar frequency to snowflake sizes and densities [e.g., *Leinonen and Szyrmer*, 2015]. Dual-frequency radar retrievals have been found to be clearly superior to single-frequency radar retrievals and to provide additional constraints to PSD parameters [*Matrosov*, 1998; *Hogan et al.*, 2000; *Liao et al.*, 2005; *Szyrmer and Zawadzki*, 2014].

By comparing various snow particle scattering models, *Kneifel et al.* [2011] found that the dual wavelength signatures increasingly depend on the particle habit when the characteristic size of the PSD increases. They suggested that the addition of a third radar frequency (e.g., the combination of Ku, Ka, and W bands) has the potential both of distinguishing between different snowflake classes, like aggregates and spheroidal particles, and of improving the retrieval of the characteristic size or width of the PSD. Subsequent triple-frequency observations, both airborne [*Leinonen et al.*, 2012; *Kulie et al.*, 2014] and ground based [*Stein et al.*, 2015; *Kneifel et al.*, 2015], confirmed the existence of distinct scattering regimes in the triple-frequency space similar to those predicted by the various scattering models. The first observational evidence for a direct link of these regimes to snowfall properties like bulk snowfall density, habit, and median volume diameter (i.e., the diameter which partitions the PSD in two equal volume parts) has recently been shown by *Kneifel et al.* [2015]. A general conclusion of these triple-frequency studies is that spheroidal scattering approximations that make use of an effective medium approximation for the snow refractive index are incapable of reproducing the observed variability in the triple-frequency space. Simulations with the computationally more expensive discrete dipole approximation (DDA) for various aggregates [*Tyynelä and Chandrasekar*, 2014; *Leinonen and Moisseev*, 2015] and rimed particles [*Tyynelä and Chandrasekar*, 2014; *Leinonen and Szyrmer*, 2015] are in general found to be superior in fitting the observed range of triple-frequency signatures and their dependence on bulk snowfall density.

Profiling cloud radars routinely record the radar Doppler spectrum and its moments such as the equivalent radar reflectivity factor Z_e (hereafter reflectivity) or the mean Doppler velocity (MDV). The radar Doppler

spectrum is the distribution of the return power over a range of Doppler velocities. Its shape is controlled by the convoluted effect of the PSD shape, the particle backscattering cross sections and fall velocities, small-scale turbulence, and transverse and radial wind [*Doviak and Zrnic*, 1993]. Profiling radars with narrow antenna beamwidth and short dwell time minimizes the role of turbulence, and thus, the radar Doppler spectrum represents the distribution of backscattered energy from small (slow) to large (fast-falling) scatterers [e.g., *Kollias et al.*, 2002; *Luke and Kollias*, 2013]. For beam-matched dual-frequency radar systems, the shapes of the radar Doppler spectra are expected to match in the velocity region where the particles behave like Rayleigh scatterers at both frequencies. *Tridon et al.* [2013] showed this spectral matching for rain and explained that differences in this region can be utilized to estimate differential attenuation between the two frequencies. After correcting for these differential attenuation or miscalibration effects, the remaining differences between the two spectra are only found at higher velocities where Mie scattering effects cause the spectra to deviate. This separation in the spectral domain has been further exploited in *Tridon and Battaglia* [2015] to simultaneously retrieve raindrop size distributions and air state parameters like vertical wind and broadening caused by turbulence and wind shear.

Unlike rain, the Doppler spectra obtained from snow particles are much narrower [*Zawadzki et al.*, 2001; *Spek et al.*, 2008] due to the smaller dynamic range of terminal fall velocities and the more ambiguous relation between particle size and terminal fall velocity caused by the large natural variability in particle habits and densities [*Locatelli and Hobbs*, 1974; *Mitchell and Heymsfield*, 2005]. To the author's knowledge, this study presents the first analysis of triple-frequency (X, Ka, and W bands) Doppler spectra of snowfall which have been collected during a recent field campaign in Finland. The data set, spectral quality control, and correction procedures are discussed in section 2. The theoretical concept of dual spectral and backscattering ratios is introduced in section 3 followed by an analysis of the observed signatures from unrimed and rimed snow aggregates. In section 4, a new technique for utilizing triple-frequency spectra to validate snow scattering models is presented. Finally, an outlook for applications of triple-frequency spectra for retrieving snowfall microphysics is presented in section 5.

2. Data Set and Methods

We focus our analysis on a short time period (23:00–23:15 UTC) during a snowfall event on 21 February 2014. The observations were recorded during the Biogenic Aerosols Effects on Clouds and Climate (BAECC) field campaign at the Hyytiälä Forestry Field site, Finland (61°50′37″N, 24°17′15″E, 150 m MSL). As part of BAECC campaign, the US Department of Energy Atmospheric Radiation Measurement (ARM) program deployed the second Mobile Facility from 1 February to 12 September 2014.

A detailed description of the entire snowfall event, the triple-frequency reflectivity signatures, and their relation to ground-based in situ measurements can be found in *Kneifel et al.* [2015]. The snowfall event was characterized by relatively mild temperatures of −2°C close to the ground and a transition of snowfall type from rimed aggregates to large (up to 15 mm) low-density aggregates accompanied by a strong reduction of liquid water path (LWP) from 300 to 50 gm^{-2}. At altitudes below 3.5 km and after 23:00 UTC, when the LWP already decreased to 150 gm^{-2}, the fields of reflectivity and MDV became rather homogeneous and the former fall streak structures, analyzed in detail in *Kalesse et al.* [2015] and associated to riming processes, almost completely disappeared.

2.1. Attenuation and Offset Corrections

The radar data analyzed in this study were recorded by the dual-frequency (X/Ka) scanning ARM cloud radar (X/Ka-SACR, *Kollias et al.* [2014]) and the W band ARM cloud radar (MWACR) during zenith pointing observations. The procedures applied to correct for atmospheric attenuation and relative radar calibration offsets are identical to those described in *Kneifel et al.* [2015]. The data analyzed within this study are taken from the lowest 2 km; the maximum total two-way attenuation due to water vapor, liquid water, and snowfall up to the top of this layer were estimated to be 2.5, 0.6, and lower than 0.1 dB at W, Ka, and X bands, respectively.

2.2. Radar Volume Matching and Beam Alignment

For the analysis of multifrequency Doppler spectra, a careful matching of the radar volumes is a critical but also a challenging task. The different radars were configured to optimize temporal and spatial matching [see *Kneifel et al.*, 2015, Table 1], but a few limitations still exist which we will discuss in the following.

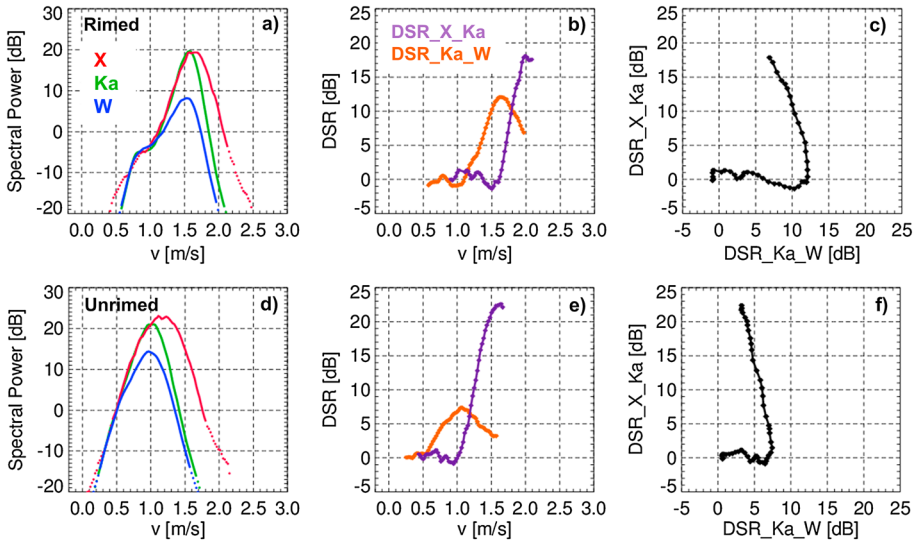

Figure 1. (a and d) Examples of triple-frequency (X, Ka, and W bands) radar Doppler spectra from a snowfall event at Hyytiälä, Finland, recorded on 21 February 2014 at 1705 m above ground level. The example in Figure 1a (23:01 UTC) is from a time period associated to rimed aggregates, while Figure 1d (23:10) shows observed spectra from unrimed snow aggregates. The Doppler velocity v is defined to be positive for particles moving toward the radar. The dual spectral ratios (DSR) are derived for X-Ka (purple) and Ka-W (orange) band for radar signal-to-noise ratios larger than 10 dB (indicated by the solid lines in Figures 1a and 1d). (b and e) DSRs shown as a function of Doppler velocity and (c and f) plotted as a function of each other.

The temporal sampling and averaging of all three systems was set to 2 s. The range gate spacing of the MWACR is 5 m larger compared to the X/Ka-SACR. Also, the range gate centers can sometimes deviate up to 16 m depending on altitude. Therefore, we selected only range gates for which the difference of the range centers was less than 5 m; this is, for example, the case for ranges of 1255 m, 1325 m, 1555 m, or 1705 m.

While the radar half-power beam widths of the Ka-SACR and MWACR are similar (0.33° and 0.38°, respectively), the X-SACR beam width of 1.27° is 3 to 4 times larger. The different beam widths can affect the spectra in two ways. First, turbulence, wind shear, and horizontal wind can lead to a symmetrical broadening of the spectra [*Doviak and Zrnic*, 1993], which increases with larger beam width and pulse length. Second, the spectra obtained from different beam widths are not related to exactly the same radar beam volume and, thus, correspond at least partly to different snowflake populations.

The effect of different spectral broadening can be detected by overlaying the three spectra. In turbulent (e.g., lowest 500 m) or high wind shear areas of the cloud, the X-SACR spectra are found to be symmetrically broader compared to MWACR and Ka-SACR spectra. In areas of the cloud with low turbulence and negligible wind shear (e.g., between 1.2 km and 1.7 km), however, we often find all three spectra almost perfectly matching at the low-velocity flank while significantly deviating at higher velocities due to differential scattering effects of larger snowflakes (Figures 1a and 1d). This proper matching of the spectra on the low-velocity side is a strong indicator that dynamical broadening effects in these particular regions of the cloud are sufficiently small, i.e., smaller than the spectral resolution of 2 cm s^{-1}. Simulation experiments with a radar Doppler spectrum forward operator as used in *Maahn et al.* [2015] revealed that matched spectra in the low-velocity region can be obtained for turbulent dissipation rates up to 10^{-4} m^2 s^{-3}. This value is in the upper range of dissipation rates (10^{-6} to 10^{-3} m^2 s^{-3}) typically found in arctic mixed phase clouds [*Shupe et al.*, 2008].

The antennas of the X/Ka-SACR are mounted on the same pedestal leading to very well aligned beams. As a result, the spectra of the X/Ka-SACR are found to be always very well matched in the low-velocity region of the spectra and no correction or shifting is needed. The MWACR was mounted on a container 17 m apart from the X/Ka-SACR [see *Kneifel et al.*, 2015, Figure 1]. When comparing the Doppler spectra of the MWACR with X/Ka-SACR, we find a slight shift in the range of 0.1 to 0.3 m s^{-1} of the MWACR spectra depending on the horizontal wind speed and direction. An analysis of the MDV differences between X/Ka-SACR and MWACR together with wind profile information from radio soundings revealed a small mispointing of the MWACR of 1° in elevation. Therefore, we corrected the MWACR spectra by shifting each MWACR spectrum until the best

match with the low-velocity (Rayleigh scattering) part of the Ka-SACR spectrum was reached. For the fit, we used the part of the spectrum with velocities smaller than 0.7 m s^{-1} and with spectral signal-to-noise ratios larger than 10 dB at both frequencies. Because the focus of this study is on scattering signatures embedded in the triple-frequency radar Doppler spectra shapes, no additional temporal averaging of the Doppler spectra is attempted [*Luke and Kollias*, 2013]. The original 2 s temporally resolved spectra are analyzed, and only a low-pass boxcar filter has been applied to remove some remaining high-frequency variations (particularly in the X-SACR spectra). The spectra from Ka-SACR and MWACR have also been interpolated onto the slightly finer velocity resolution of the X-SACR (2 cm s^{-1}).

3. Analysis of Multifrequency Doppler Spectra

The Doppler spectrum $S_\lambda(v)$ (in $mm^6\,m^{-3}(m\,s^{-1})^{-1}$) in a quiet air environment can be calculated with the particle size distribution $N(D)$ (in m^{-4}) and the particle's backscattering cross section $\sigma_{bsc}(\lambda, D)$ (in mm^2) which is usually described as a function of particle maximum size D (in meters) and radar wavelength λ (in meters).

$$S_\lambda(v) = \frac{\lambda^4}{\pi^5 |K_w|^2} N(D)\sigma_{bsc}(\lambda, D)\frac{dD}{dv} = \frac{\lambda^4}{\pi^5 |K_w|^2} N(v)\sigma_{bsc}(\lambda, v). \quad (1)$$

$|K_w|^2$ is related to the complex refractive index of liquid water, and values of 0.93, 0.88, and 0.70 are used in the original X-SACR, Ka-SACR, and MWACR data files, respectively. Similar to *Stein et al.* [2015], we normalized the Ka and W band data to $|K_w|^2$ values of 0.93 in order to ensure the same reflectivity for ice particles being Rayleigh scatterers at all three frequencies. The term $\frac{dD}{dv}$ represents the transformation from the diameter space into the terminal velocity space and can be derived from a velocity-size relation, often described as a power law of the form $v(D) = \alpha D^\beta$, with α and β being empirical parameters.

A real measured spectrum $Sr_\lambda(v, r)$ at range r is also affected by the path-integrated two-way attenuation $A_\lambda(r)$, caused by gases, liquid water, and frozen hydrometeors such that $Sr_\lambda(v, r) = S_\lambda(v, r)A_\lambda(r)^{-1}$. As mentioned earlier, the data analyzed have been carefully corrected for relative radar miscalibration and atmospheric attenuation as described in *Kneifel et al.* [2015]. The largest remaining uncertainty in the attenuation correction is the unknown liquid water content profile. However, during the time period we analyze in this study, LWP is always lower than 150 g m^{-2} and thus, the total two-way attenuation at W band is lower than 1.2 dB. Therefore, we assume the remaining attenuation correction uncertainties to be small compared to the scattering component and will neglect the attenuation component in the following discussion.

The dual wavelength ratio $DWR_{\lambda_1,\lambda_2}$ (in the following we will also use the radar band indicators X, Ka, and W instead of λ) is the ratio of the effective reflectivity factors (in linear units):

$$DWR_{\lambda_1,\lambda_2} = \frac{\int_{-v_{Nyq}}^{v_{Nyq}} S_{\lambda_1}(v)dv}{\int_{-v_{Nyq}}^{v_{Nyq}} S_{\lambda_2}(v)dv} = \frac{Z_{e,\lambda_1}}{Z_{e,\lambda_2}}. \quad (2)$$

By building the ratio of the ideal quiet air spectra as defined in (1) for two different wavelengths (after normalization with $|K_w|^2$), we obtain

$$DBR_{\lambda_1,\lambda_2}(v) = \left(\frac{\lambda_1}{\lambda_2}\right)^4 \frac{\sigma_{bsc}(\lambda_1, v)}{\sigma_{bsc}(\lambda_2, v)}. \quad (3)$$

We may call $DBR_{\lambda_1,\lambda_2}$ the normalized dual backscattering ratio because for Rayleigh scatterers, $DBR_{\lambda_1,\lambda_2} = 1$. As mentioned before, in a real spectrum dynamical effects like turbulence or wind shear broaden the spectrum and smear the microphysical signatures in $S_\lambda(v)$ while attenuation reduces the overall amplitude of $S_\lambda(v)$. If the smearing effects are sufficiently small and if the velocity resolution of the radar δv is fine enough so that $N(v) \approx N(v + \delta v)$ and $\sigma_{bsc}(\lambda, v) \approx \sigma_{bsc}(\lambda, v + \delta v)$, the dual spectral ratio $DSR_{\lambda_1,\lambda_2}(v)$ approximates $DBR_{\lambda_1,\lambda_2}$:

$$DSR_{\lambda_1,\lambda_2}(v) = \frac{Sr_{\lambda_1}(v, r)}{Sr_{\lambda_2}(v, r)} \approx DBR_{\lambda_1,\lambda_2}(v, r). \quad (4)$$

Differential attenuation $A_{\lambda_2}/A_{\lambda_1}$ is assumed to be equal to 1 in (4) due to the applied attenuation corrections. We used again our radar Doppler spectrum forward operator [*Maahn et al.*, 2015] to simulate $DSR_{\lambda_1,\lambda_2}(v)$ and compared them to $DBR_{\lambda_1,\lambda_2}$ calculated with the scattering models described in section 4. We found that for dynamical conditions which produce matched spectra in the Rayleigh regime similar to our observations, the $DSR_{\lambda_1,\lambda_2}$ closely approximates the $DBR_{\lambda_1,\lambda_2}$ with maximum deviations of less than 2 dB.

3.1. Observed Triple-Frequency Spectra of Rimed and Unrimed Aggregates

Based on the measured LWP and MDV, the data set is divided into a period with (23:00–23:04 UTC) and without (23:04–23:14 UTC) clear signatures of riming. The spectra during the riming period peak at 0.5 m s^{-1} higher fall velocities (1.6 m s^{-1}) compared to the spectra from the unrimed period (Figures 1a and 1d). The spectra match well in the low-velocity region, which results in a flat Rayleigh plateau when plotting the DSRs as a function of Doppler velocity (Figures 1b and 1e). The Rayleigh plateaux close to 0 dB confirm the suitability of the corrections for attenuation and offsets applied. For the X/Ka combination, the plateau region can be found within a wider velocity range due to the wider size range of particles that are still Rayleigh scatterers at both frequencies. The typical particle size range where the scattering models, described in section 4, predict deviations from the Rayleigh region between 2 and 2.5 dB in terms of BSR are provided in Table S1 in the supporting information.

If the DSRs could be expressed as a function of particle size, that would allow to compare the DSRs directly to the backscattering ratios from scattering models. This requires an accurate estimate of the vertical wind and the velocity-size relation. For rainfall, the relation between raindrop size and terminal velocity is well known and the raindrop backscattering properties can also be accurately calculated [*Tridon and Battaglia*, 2015]. Specific scattering signatures can be attributed to specific raindrop sizes and terminal velocities which allows to correct for vertical air motion [*Kollias et al.*, 2002]. For snowfall, no similarly well-constrained relations exist. The shift due to vertical air motion can only be corrected for if an air tracer like small supercooled liquid water droplets are present and if their spectral signal can be distinguished from the ice and snow spectrum [*Shupe et al.*, 2008; *Kalesse et al.*, 2015]. The velocity-size relation of snowfall is highly variable and depends not only on size but also on the degree of riming, the overall particle density, and the horizontal cross section of the particle [e.g., *Heymsfield and Westbrook*, 2010; *Szyrmer and Zawadzki*, 2010]. If the backscattering properties of the snowfall particles could be well characterized, this would in turn allow to use the DSR to retrieve the velocity-size relation. Currently, scattering simulations and triple-frequency observations indicate a large range of possible snowfall scattering properties and our knowledge on how to link the scattering properties to snowfall properties is still poor.

One first application of the triple-frequency spectra is to use them for the validation of scattering models even if vertical air motion and the velocity-size relation are unknown. When plotting all the spectral points of $DSR_{Ka,W}$ against $DSR_{X,Ka}$ in correspondence to each backscattering volume under low-turbulence conditions (Figures 1c and 1f), we obtain a unique curve that is characteristic of the specific snowfall backscattering ratios but independent on the snow particle velocity. A sharp turning point, i.e., the value of $DSR_{Ka,W}$ where $DSR_{X,Ka}$ starts to increase strongly, is found both for the period of riming and of unrimed aggregates. For the spectra of rimed particles, the turning point is at 12 dB and is shifted by around 4 dB toward larger $DSR_{Ka,W}$ values compared to the period dominated by unrimed aggregates. In the unrimed case, the turning point is related to Doppler velocities of 1.1 m s^{-1}, while it is shifted to 1.6–1.7 ms^{-1} in the rimed cases.

Due to the aforementioned difficulties to relate the DSRs to particle sizes, we focus the following comparison with scattering models on the $DSR_{Ka,W}$-$DSR_{X,Ka}$ curves. In order to obtain a more robust signature, we extended the analysis to the entire time period and altitudes at which matched spectra are found (Figures 2a and 2c). The total number of spectra during the riming period ($N = 17$) is much smaller compared to the unrimed cases ($N = 109$). This is due to the shorter duration of the riming period, but it is also caused by stronger dynamical broadening effects found during the riming period which leads to less sufficiently matched X-SACR spectra. Despite the different total number of spectra and the larger variability of the $DSR_{Ka,W}$-$DSR_{X,Ka}$ curves during the riming period, the median curves clearly reveal the turning point to be shifted by 5–6 dB to larger $DSR_{Ka,W}$ values in case of rimed particles (Figures 2a and 2c).

The X-SACR MDV (color coding in Figure 2) confirms that the majority of spectra with a turning point shifted to larger $DSR_{Ka,W}$ are affected by riming, as indicated by MDVs considerably larger than 1.3 m s^{-1}. The DWR derived from spectra with enhanced MDVs also populate a region in the triple-frequency space (Figure 2b) that has been identified in *Kneifel et al.* [2015] to be connected to riming in the comparison with in situ observations.

Except for a few outliers, the turning point always coincides with the maximum $DSR_{Ka,W}$ value which can be reached by the underlying particle population. Those particles that cause the maximum $DSR_{Ka,W}$ are just transitioning from Rayleigh into Mie scattering regime at Ka band; this is visible in the steeply increasing $DSR_{X,Ka}$

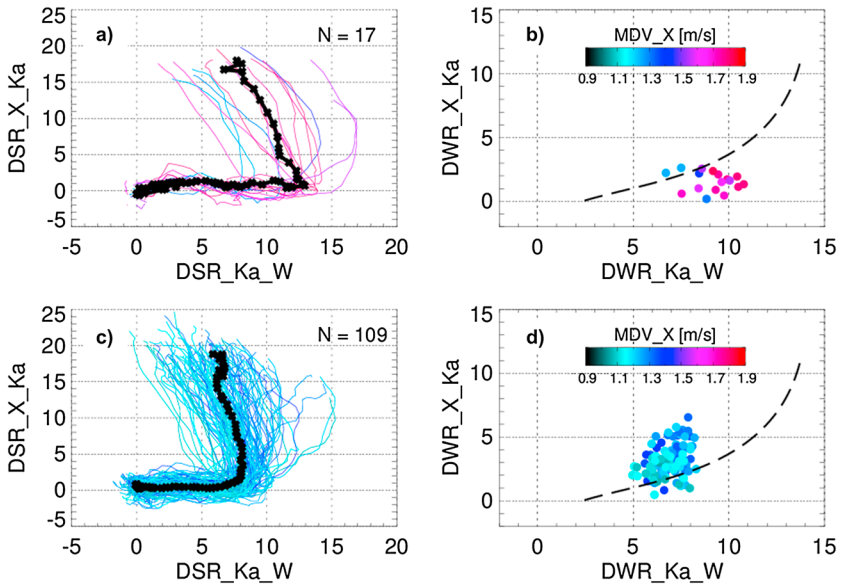

Figure 2. DSRs and DWRs derived for all selected triple-frequency spectra (a and b) during the riming period and (c and d) during the period of unrimed snow aggregates. The color coding denotes the mean Doppler velocity derived from the X band spectra. The black solid lines in Figures 2a and 2c are the mean of the $DSR_{Ka,W}$-$DSR_{X,Ka}$ curves; the black dashed lines in Figures 2b and 2d indicate the average $DWR_{Ka,W}$-$DWR_{X,Ka}$ region occupied by a large ensemble of spheroidal scattering approximations and particle size distributions similar to *Kneifel et al.* [2015].

values. It also seems that the $DSR_{Ka,W}$ from the unrimed aggregates only slightly decreases from the turning point to larger Doppler velocities (Figure 2c), while a stronger decrease in the range of 5 dB for the median curve is found for the rimed particles (Figure 2a).

A possible explanation for these specific $DSR_{Ka,W}$ maxima can be found when relating the scattering properties to the particles' fractal dimension d_f. *Stein et al.* [2015] found a saturation value for $DWR_{Ka,W}$ of 8 dB for triple-frequency measurements of thick ice clouds. Assuming that the particles can be approximated well with the Rayleigh-Gans approximation [*Bohren and Huffman*, 1983], they relate this saturation values to $d_f = 2$, a value typically found for fractal aggregates [*Westbrook et al.*, 2006]. For $d_f = 3$, which can be assumed as upper limit for rimed particles, their relation predicts a saturation of $DWR_{Ka,W}$ at 13 dB. One implicit assumption in *Stein et al.* [2015] is that most of the particles within the radar sampling volume contributing to the reflectivity have the same d_f. The DSR, however, allows to separate the contributions of the different size classes. In Appendix 1 we show that $DWR_{Ka,W} \leq \max(DSR_{Ka,W})$, which is also confirmed by the observations in Figure 2. It is striking that the saturation values predicted by the relation in *Stein et al.* [2015] for $d_f = 2$ and $d_f = 3$ are very close to the maximum $DSR_{Ka,W}$ values found for the turning points in the $DSR_{Ka,W}$-$DSR_{X,Ka}$ space during the unrimed and rimed periods. Given that the Rayleigh-Gans approximation and the concept of fractal dimension is valid for all particle size classes within the radar volume, the DSRs bear the potential to derive d_f as a function of Doppler velocity and, therefore, particle size.

4. Comparison to Scattering Models

The near independence of the DSR to the underlying PSD makes them extremely useful for validating snow scattering models. The selected triple-frequency DSRs are compared against the DBRs of unrimed and rimed aggregates calculated with the discrete dipole approximation (DDA, *Leinonen and Szyrmer* [2015] using ADDA [*Yurkin and Hoekstra*, 2011]), the self-similar Rayleigh-Gans theory (SSRG, *Hogan and Westbrook* [2014]) and T-Matrix calculations from *Leinonen and Szyrmer* [2015], generated using the code of *Mishchenko and Travis* [1998] and *Leinonen* [2014], which closely correspond to the microphysical properties of their DDA aggregates in terms of mass and radius of gyration. *Leinonen and Szyrmer* [2015] provided scattering calculations for three different riming models from which we only use the two aggregate riming models (types A and B). The scattering properties of the two models are overall very similar, and by combining them we ensure a larger number of particles per Doppler velocity bin which makes the resulting $DSR_{Ka,W}$-$DSR_{X,Ka}$ curve more representative for a real radar volume. We then selected completely unrimed aggregates and the second

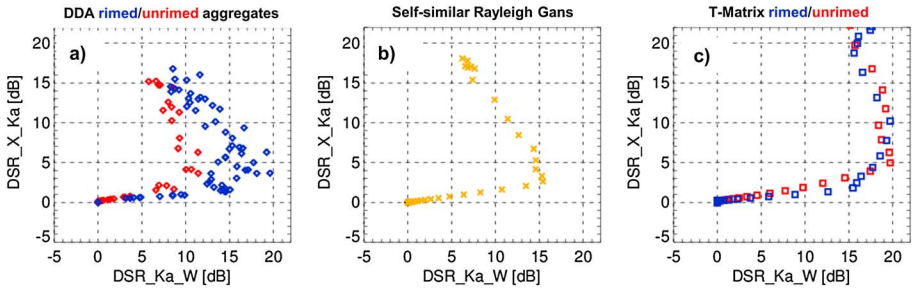

Figure 3. (a) Dual backscattering ratios (DBR) averaged to the radar Doppler velocity resolution (2 cm s^{-1}) calculated with the discrete dipole approximation (DDA) for unrimed (red) and rimed (blue) snow aggregates [*Leinonen and Szyrmer*, 2015]. (b) As in Figure 3a, but DBRs are calculated with the self-similar Rayleigh-Gans theory [*Hogan and Westbrook*, 2014] assuming unrimed aggregates of bullet rosettes and columns. (c) DBRs based on T-Matrix calculations in *Leinonen and Szyrmer* [2015] for spheroids matching closely the microphysical and backscattering properties of the rimed (blue) and unrimed (red) DDA aggregates shown in Figure 3a.

heaviest rimed aggregates as well as their spheroidal counterparts. This selection was found to fit our observations best. $DSR_{Ka,W}$-$DSR_{X,Ka}$ curves calculated from a different selection of rimed particles mainly result in a horizontal shift between the two curves seen in Figure 3a.

The size-dependent backscattering properties have been converted into the terminal fall velocity space using averaged *v-D* relations from the in situ observations during the riming ($\alpha = 0.9, \beta = 0.4$) and nonriming ($\alpha = 0.7, \beta = 0.2$) periods. Then they have been averaged to the radar Doppler velocity resolution. Of all scattering models, the DDA scattering calculations (Figure 3a) reveal the best agreement with the observations. The unrimed aggregates show a very similar sharp turning point at a $DSR_{Ka,W}$ of 9 to 10 dB. The turning point of the rimed aggregates, however, is 5 dB larger in remarkably close agreement with the observations (Figures 2a and 2c). Interestingly, also the change of the slope of $DSR_{Ka,W}$ above the turning point and the larger variability of DSR for rimed aggregates is very similar to the observations.

The spheroids for the T-Matrix computations presented in *Leinonen and Szyrmer* [2015] were designed to optimally match the aggregate's backscattering properties which resulted in a general good agreement of their signatures in the $DWR_{Ka,W}$-$DWR_{X,Ka}$ space. Hence, it is quite surprising that their $DSR_{Ka,W}$-$DSR_{X,Ka}$ signatures (Figure 2c) significantly deviate from their DDA counterparts and that they differ the most from the observed DSR curves. Further, the turning point on the $DSR_{Ka,W}$ axis is overestimated and found at 15 to 20 dB; it also remains in this region for larger particles. Particularly, the observed shift between rimed and unrimed particles cannot be found in the T-Matrix simulations.

The DSR curve for the self-similar Rayleigh-Gans approximation (Figure 3b) for unrimed aggregates of bullet rosettes or columns given in *Hogan and Westbrook* [2014] is able to reproduce the observed shape reasonably well. However, it overestimates the maximum observed $DSR_{Ka,W}$ by 5 dB and also causes a reduction of $DSR_{Ka,W}$ for larger aggregates by 8 dB, which is much larger than the observations of unrimed aggregates suggest. It would be interesting to investigate in future studies whether a better match can be achieved if dendrites or sector snowflakes would be used as primary particles for the aggregates.

5. Conclusions

In this study, we analyzed for the first time collocated triple-frequency (X, Ka, and W bands) Doppler spectra for a snowfall event including a transition from rimed to unrimed snow aggregates. Despite challenges associated to the proper matching of the radar volumes and correcting for attenuation and calibration offsets, the comparison revealed that under low-turbulence conditions, a matching of all three spectra in the low-velocity or Rayleigh part of the spectrum is feasible. Under these conditions, the derived dual spectral ratios approximate the dual backscattering ratios which can be directly calculated from snow scattering models. A combination of $DSR_{Ka,W}$ and $DSR_{X,Ka}$ is found to provide a unique curve which is not strongly dependent on a precise characterization of the PSD or the velocity-size relation but which shows significant differences between rimed and unrimed particles. This curve can be directly compared to scattering models which show considerable differences between each other; the best agreement to the observations is found for calculations using the discrete dipole approximation for unrimed and rimed dendrite aggregates.

If the velocity-size relation can be further constrained (e.g., by in situ observations), the dual spectral ratios can be expressed as a function of particle size which allows further constraints to scattering models.

Appendix A: Relation Between DBR and DWR

The definitions of DWR and DBR in equations (2) and (3) show that DBR—obtained for example by measuring DSR—cannot be directly used to derive DWR. However, we can show that if $\lambda_1 \leq \lambda_2$ and $|K_w|^2$ is assumed to be the same at both wavelengths,

$$\mathrm{DWR}_{\lambda_1,\lambda_2} = \left(\frac{\lambda_1}{\lambda_2}\right)^4 \frac{\int_{-v_{\mathrm{Nyq}}}^{v_{\mathrm{Nyq}}} N(v)\mathrm{DBR}_{\lambda_1,\lambda_2}(v)\sigma_{\mathrm{bsc}}(\lambda_2,v)\mathrm{d}v}{\int_{-v_{\mathrm{Nyq}}}^{v_{\mathrm{Nyq}}} N(v)\sigma_{\mathrm{bsc}}(\lambda_2,v)\mathrm{d}v}$$

$$\leq \left(\frac{\lambda_1}{\lambda_2}\right)^4 \frac{\max(\mathrm{DBR}_{\lambda_1,\lambda_2}(v)) \int_{-v_{\mathrm{Nyq}}}^{v_{\mathrm{Nyq}}} N(v)\sigma_{\mathrm{bsc}}(\lambda_2,v)\mathrm{d}v}{\int_{-v_{\mathrm{Nyq}}}^{v_{\mathrm{Nyq}}} N(v)\sigma_{\mathrm{bsc}}(\lambda_2,v)\mathrm{d}v} = \max\left(\mathrm{DBR}_{\lambda_1,\lambda_2}(v)\right).$$

Acknowledgments

Work carried out by S.K. was supported by a Postdoctoral Fellowship from the German Academic Exchange Service (DAAD); additional funding for S.K. and P.K. was provided by the U.S. Department of Energy Atmospheric System Research (ASR) program. The research of J.L. was carried out at the Jet Propulsion Laboratory, California Institute of Technology, under contract with NASA. The development of the radar forward operator was supported by the German Federal Ministry of Education and Research (BMBF) within the High Definition Clouds and Precipitation for advancing Climate Prediction ($(HD(CP)^2)$) project (01LK1211C). We thank Robin Hogan for providing his code to compute SSRG. We also acknowledge valuable discussions with Chris Westbrook, Thorwald Stein, and Andrew Barrett. All remote sensing and in situ data from the BAECC campaign used in this study are available from the ARM data archive at http://www.archive.arm.gov. The processed spectral data are available on request from the corresponding author.

References

Bohren, C. F., and D. R. Huffman (1983), *Absorption and Scattering of Light by Small Particles*, John Wiley, New York.

Doviak, R. J., and D. S. Zrnic (1993), *Doppler Radar and Weather Observations*, 2nd ed., Academic Press, San Diego, Calif.

Heymsfield, A. J., and C. D. Westbrook (2010), Advances in the estimation of ice particle fall speeds using laboratory and field measurements, *J. Atmos. Sci.*, *67*(8), 2469–2482, doi:10.1175/2010JAS3379.1.

Hogan, R. J., and C. D. Westbrook (2014), Equation for the microwave backscatter cross section of aggregate snowflakes using the self-similar rayleigh-gans approximation, *J. Atmos. Sci.*, *9*, 3292–3301.

Hogan, R. J., A. J. Illingworth, and H. Sauvageot (2000), Measuring crystal size in cirrus using 35-and 94-GHz radars, *J. Atmos. Ocean. Technol.*, *17*(1), 27–37.

Kalesse, H., W. Szyrmer, S. Kneifel, P. Kollias, and E. Luke (2015), Fingerprints of a riming event on cloud radar Doppler spectra: Observations and modeling, *Atmos. Chem. Phys. Discuss.*, *15*(20), 28,619–28,658, doi:10.5194/acpd-15-28619-2015.

Kneifel, S., A. von Lerber, J. Tiira, D. Moisseev, P. Kollias, and J. Leinonen (2015), Observed relations between snowfall microphysics and triple-frequency radar measurements, *J. Geophys. Res. Atmos.*, *120*(12), 6034–6055, doi:10.1002/2015JD023156.

Kneifel, S., M. S. Kulie, and R. Bennartz (2011), A triple-frequency approach to retrieve microphysical snowfall parameters, *J. Geophys. Res.*, *116*, D11203, doi:10.1029/2010JD015430.

Kollias, P., B. Albrecht, and F. Marks (2002), Why Mie? Accurate observations of vertical air velocities and raindrops using a cloud radar, *Bull. Am. Meteorol. Soc.*, *83*(10), 1471–1483, doi:10.1175/BAMS-83-10-1471.

Kollias, P., I. Jo, P. Borque, A. Tatarevic, K. Lamer, N. Bharadwaj, K. Widener, K. Johnson, and E. E. Clothiaux (2014), Scanning ARM cloud radars. Part II: Data quality control and processing, *J. Atmos. Oceanic Technol.*, *31*(3), 583–598, doi:10.1175/JTECH-D-13-00045.1.

Kulie, M. S., and R. Bennartz (2009), Utilizing spaceborne radars to retrieve dry snowfall, *J. Appl. Meteorol. Climatol.*, *48*(12), 2564–2580, doi:10.1175/2009JAMC2193.1.

Kulie, M. S., M. J. Hiley, R. Bennartz, S. Kneifel, and S. Tanelli (2014), Triple-frequency radar reflectivity signatures of snow: Observations and comparisons with theoretical ice particle scattering models, *J. Appl. Meteorol. Climatol.*, *53*(4), 1080–1098.

Leinonen, J. (2014), High-level interface to T-matrix scattering calculations: Architecture, capabilities and limitations, *Opt. Express*, *22*(2), 1655–1660, doi:10.1364/OE.22.001655.

Leinonen, J., and D. Moisseev (2015), What do triple-frequency radar signatures reveal about aggregate snowflakes?, *J. Geophys. Res. Atmos.*, *120*(1), 229–239, doi:10.1002/2014JD022072.

Leinonen, J., and W. Szyrmer (2015), Radar signatures of snowflake riming: A modeling study, *Earth Space Sci.*, *2*(8), 346–358, doi:10.1002/2015EA000102.

Leinonen, J., S. Kneifel, D. Moisseev, J. Tyynelä, S. Tanelli, and T. Nousiainen (2012), Evidence of nonspheroidal behavior in millimeter-wavelength radar observations of snowfall, *J. Geophys. Res.*, *117*, D18205, doi:10.1029/2012JD017680.

Liao, L., R. Meneghini, T. Iguchi, and A. Detwiler (2005), Use of dual-wavelength radar for snow parameter estimates, *J. Atmos. Oceanic Technol.*, *22*(10), 1494–1506, doi:10.1175/JTECH1808.1.

Locatelli, J. D., and P. V. Hobbs (1974), Fall speeds and masses of solid precipitation particles, *J. Geophys. Res.*, *79*(15), 2185–2197, doi:10.1029/JC079i015p02185.

Luke, E. P., and P. Kollias (2013), Separating cloud and drizzle radar moments during precipitation onset using Doppler spectra, *J. Atmos. Oceanic Technol.*, *30*(8), 1656–1671, doi:10.1175/JTECH-D-11-00195.1.

Maahn, M., U. Loehnert, P. Kollias, R. C. Jackson, and G. M. McFarquhar (2015), Developing and evaluating ice cloud parameterizations for forward modeling of radar moments using in situ aircraft observations, *J. Atmos. Oceanic Technol.*, *32*(5), 880–903, doi:10.1175/JTECH-D-14-00112.1.

Matrosov, S. Y. (1998), A dual-wavelength radar method to measure snowfall rate, *J. Appl. Meteorol.*, *37*(11), 1510–1521.

Mishchenko, M. I., and L. D. Travis (1998), Capabilities and limitations of a current FORTRAN implementation of the T-matrix method for randomly oriented, rotationally symmetric scatterers, *J. Quant. Spectros. Radiat. Transfer*, *60*(3), 309–324, doi:10.1016/S0022-4073(98)00008-9.

Mitchell, D. L., and A. J. Heymsfield (2005), Refinements in the treatment of ice particle terminal velocities, highlighting aggregates, *J. Atmos. Sci.*, *62*(5), 1637–1644, doi:10.1175/JAS3413.1.

Shupe, M. D., P. Kollias, M. Poellot, and E. Eloranta (2008), On deriving vertical air motions from cloud radar Doppler spectra, *J. Atmos. Oceanic Technol.*, *4*, 547–557, doi:10.1175/2007JTECHA1007.1.

Spek, A. L. J., C. M. H. Unal, D. N. Moisseev, H. W. J. Russchenberg, V. Chandrasekar, and Y. Dufournet (2008), A new technique to categorize and retrieve the microphysical properties of ice particles above the melting layer using radar dual-polarization spectral analysis, *J. Atmos. Oceanic Technol.*, *25*(3), 482–497, doi:10.1175/2007JTECHA944.1.

Stein, T. H. M., C. D. Westbrook, and J. C. Nicol (2015), Fractal geometry of aggregate snowflakes revealed by triple-wavelength radar measurements, *Geophys. Res. Lett.*, *42*(1), 176–183, doi:10.1002/2014GL062170.

Szyrmer, W., and I. Zawadzki (2010), Snow studies. part II: Average relationship between mass of snowflakes and their terminal fall velocity, *J. Atmos. Sci.*, *67*(10), 3319–3335, doi:10.1175/2010JAS3390.1.

Szyrmer, W., and I. Zawadzki (2014), Snow studies. part IV: Ensemble retrieval of snow microphysics from dual-wavelength vertically pointing radars, *J. Atmos. Sci.*, *71*(3), 1171–1186, doi:10.1175/JAS-D-12-0286.1.

Szyrmer, W., A. Tatarevic, and P. Kollias (2012), Ice clouds microphysical retrieval using 94-GHz Doppler radar observations: Basic relations within the retrieval framework, *J. Geophys. Res.*, *117*, D14203, doi:10.1029/2011JD016675.

Tridon, F., and A. Battaglia (2015), Dual-frequency radar Doppler spectral retrieval of rain drop size distributions and entangled dynamics variables, *J. Geophys. Res. Atmos.*, *120*(11), 5585–5601, doi:10.1002/2014JD023023.

Tridon, F., A. Battaglia, and P. Kollias (2013), Disentangling mie and attenuation effects in rain using a Ka-W dual-wavelength Doppler spectral ratio technique, *Geophys. Res. Lett.*, *40*(20), 5548–5552, doi:10.1002/2013GL057454.

Tyynelä, J., and V. Chandrasekar (2014), Characterizing falling snow using multifrequency dual-polarization measurements, *J. Geophys. Res. Atmos.*, *119*(13), 8268–8283, doi:10.1002/2013JD021369.

Westbrook, C., R. Ball, and P. Field (2006), Radar scattering by aggregate snowflakes, *Q. J. R. Meteorol. Soc.*, *132*(616), 897–914, doi:10.1256/qj.05.82.

Yurkin, M. A., and A. G. Hoekstra (2011), The discrete-dipole-approximation code ADDA: Capabilities and known limitations, *J. Quant. Spectros. Radiat. Transfer*, *112*(13), 2234–2247, doi:10.1016/j.jqsrt.2011.01.031.

Zawadzki, I., F. Fabry, and W. Szyrmer (2001), Observations of supercooled water and secondary ice generation by a vertically pointing X-band Doppler radar, *Atmos. Res.*, *59*, 343–359, doi:10.1016/S0169-8095(01)00124-7.